World Electric Vehicle Journal

MDPI

Article

Design, Analysis, and Comparison of Electric Vehicle Drive Motor Rotors Using Injection-Molded Carbon-Fiber-Reinforced Plastics

Huai Cong Liu *, Jang Soo Park and Il Hwan An

Hyundai-Transys, Hwaseong Powertrain R&D Center, Hyundai-Transys, 95, Hyundaikia-ro, Namyang-Eup, Hwaseong-si 18280, Republic of Korea; jspark21@hyundai-transys.com (J.S.P.); ilhwan_an@hyundai-transys.com (I.H.A.)

* Correspondence: hcliu@hyundai-transys.com; Tel.: +82-1030769989

Abstract: Due to their excellent mechanical strength, corrosion resistance, and ease of processing, carbon fiber and carbon-fiber-reinforced plastics are finding wide application in diverse fields, including aerospace, industry, and automobiles. This research explores the feasibility of integrating carbon fiber solutions into the rotors of 85-kilowatt electric vehicle interior permanent magnet synchronous motors. Two novel configurations are proposed: a carbon fiber wire-wound rotor and a carbon fiber injection-molded rotor. A finite element analysis compares the performance of these models against a basic designed rotor, considering factors like no-load back electromotive force, no-load voltage harmonics, cogging torque, load torque, torque ripple, efficiency, and manufacturing cost. Additionally, a comprehensive analysis of system efficiency and energy loss based on hypothetical electric vehicle parameters is presented. Finally, mechanical strength simulations assess the feasibility of the proposed carbon fiber composite rotor designs.

Keywords: injection-molded carbon-fiber-reinforced plastics; carbon-fiber sleeve; electric vehicle traction motor; rotor strength analysis; finite element method

Citation: Liu, H.C.; Park, J.S.; An, I.H. Design, Analysis, and Comparison of Electric Vehicle Drive Motor Rotors Using Injection-Molded Carbon-Fiber-Reinforced Plastics. *World Electr. Veh. J.* **2024**, *15*, 283. https://doi.org/10.3390/wevj15070283

Academic Editor: Peter Van den Bossche

Received: 31 May 2024
Revised: 17 June 2024
Accepted: 20 June 2024
Published: 25 June 2024

1. Introduction

With the development of the electric power industry, electric motors are increasingly finding use in electric vehicles (EVs). Tighter emission regulations are driving the demand for high-speed electric vehicle motors. These motors offer a compelling combination of high power density, high efficiency, small size, and lightweight design, thanks to the development of permanent magnet (PM) and power conversion control technology. The demand for these technologies continues to grow, and their application fields are rapidly diversifying [1–5]. In the high-speed range, the internal permanent magnet synchronous motor (IPMSM) receives a local maximum stress at the edge of the magnet pocket as the rotor rotates, and the critical speed is limited by the mechanical stress [6,7]. This raises crucial mechanical challenges, demanding significant improvements in rotor strength and stiffness. To address these challenges, researchers have investigated motors like synchronous reluctance motors (SRMs) and wound field synchronous motors (WFSMs) as potential solutions [8–10]. These motors offer benefits such as a simple rotor structure without permanent magnets, making them suitable for high-speed operation. However, limitations in material properties currently hinder their torque density, posing a barrier to their adoption in electric vehicle drive motors. One solution lies in employing high-strength non-magnetic metal sheaths like titanium alloy or stainless steel as the motor rotor sleeve [11–14]. However, this may carry the penalty of increased weight and potential eddy current losses due to their conductivity. Meanwhile, eddy current loss affects efficiency reduction, and heat loss occurs due to heat [15]. Therefore, the new carbon fibers and carbon-fiber-reinforced plastics, with their excellent mechanical strength, corrosion resistance, low electrical conductivity, and

ease of processing, offer a promising improvement solution. Recently, Tesla launched an electric motor that boasts a maximum speed of 20,000 r/min, using carbon-fiber-reinforced plastic rotor sleeves [16,17]. This is a method in which a carbon fiber tow impregnated with liquid resin is wound around a mandrel, and then heat-cured. There are two versions of this method: (1) winding the carbon fiber while it is soaking in a resin bath; and (2) winding the tow prepreg, which is impregnated with resin. When using this type of molding method, the topology shows that the rotor rib and bridge structures can be omitted. Due to the removal of the rib and bridge structures, the PM can reduce more leakage magnetic flux. Structurally, the retaining sleeve increases the strength of the rotor, but electromagnetically, it has an effect similar to an air gap, reducing the output [13,18]. In order to validate the developed construction stress and deformation analyses, rotor and sleeve strength analyses are indispensable [19]. In this paper, a new carbon fiber injection-molded structure is introduced. This is a molding method in which the raw material, a pellet of thermoplastic resin (e.g., nylon, polycarbonate) reinforced with carbon fiber is heated until it melts, and then injected into the cavity (void) of a mold. Although the mechanical properties are not as good, this molding method is suitable for molding complex shapes with short cycle times [20,21]. Meanwhile, compared with the Tesla motor's topology, the design is intended to maintain the mechanical strength of the rotor without increasing the air-gap thickness. Figure 1b shows the process diagram and finished product of injection-molded carbon fiber. First, based on the detailed electromagnetic analysis, the parameters of the three IPMSM comparison models are determined. Subsequently, the models' no-load and load capabilities are compared, in Section 2, including the no-load electromotive force, cogging torque, load speed and torque capability, efficiency, and drive cycle energy consumption comparison. Furthermore, the analysis of the rotor strength is conducted. Through the above finite element method (FEM)-aided analysis, it can be concluded that the mechanical construction is feasible and reliable. Finally, conclusions are given in Section 6.

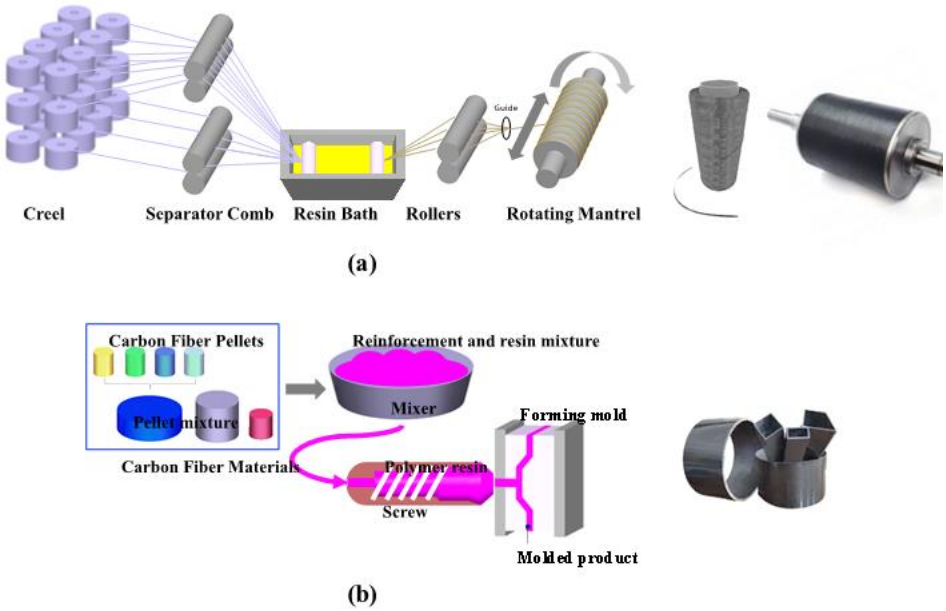

Figure 1. Carbon fiber molding manufacturing process and finished product, (**a**) Filament-winding Molding (**b**) Injection Molding.

2. Configuration and Specification

The target three-phase traction IPMSM is rated at 85 kW, with a base speed of 3000 r/min and a rated torque of 220 Nm. To analyze the characteristics of IPM motors as a function of rotor shape, the outer diameter of each rotor was fixed to ensure the same conditions and to minimize the number of variables. The typical EV traction motor designs are selected in this comparison. The structure of the basic model rotor, which

uses a "single V-shape" PM arrangement to increase the torque at start-up [22], is shown in Figure 2. The basic motor is designed as 48-slot-eight-pole with a hair-pin winding to increase torque density. The rotor lamination and pole piece lamination of model 2 are in a separate state and need to be wrapped with carbon-fiber-reinforced plastic (CFRP) sleeves. The rotor laminations of model 3 are the same as those of model 2, without ribs and bridge structures, but most importantly, this design uses a filled injection-molded CFRP material, which is fixed through the unsaturated positions (inside q-axis and inside the pole piece) in the rotor laminations. As shown in Figure 2c. Such a structure requires the rotor laminations to be completely superimposed and then fixed by injection molding. Therefore, it cannot be made into a skewed rotor structure. Meanwhile, the injection-molded CFRP materials on the upper and lower sides of the rotor lamination after injection molding are used as the rotor end-plate for fixing and rotor balancing process.

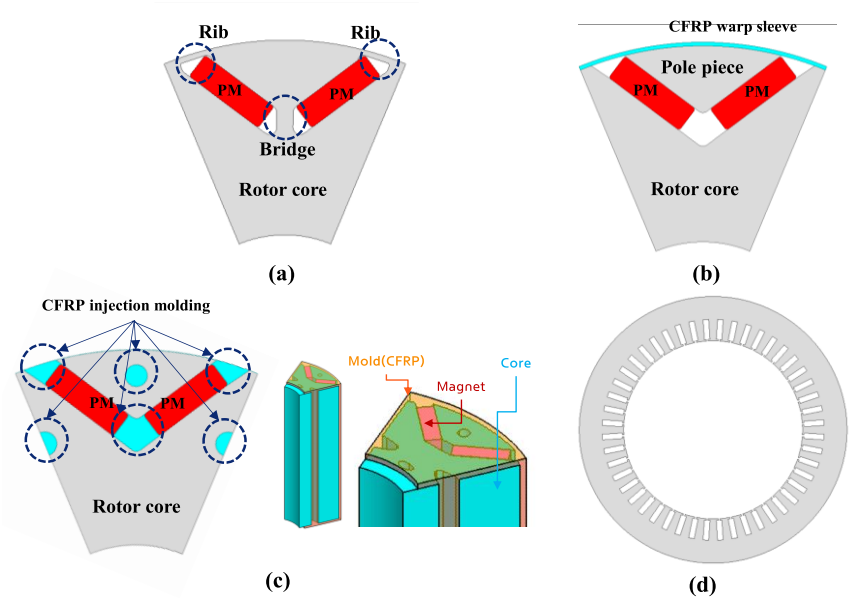

Figure 2. Cross-sections of the IPMSM rotor (1/8 model) and stator (full model). (**a**) Basic model. (**b**) Model 2: CFRP-wrapped rotor (**c**) Model 3: rotor with injection-molded CFRP. (**d**) Forty-eight parallel slots, hair-pin stator.

Table 1 presents the specifications of the models used in this study. In the design of an IPMSM for EV applications, such as efficiency at the driver cycle, total weight, cost, rotor strength analysis and torque-ripple requirements, the analysis conditions for the comparison are as follows.

(1) All three models share the same stator specifications, graded PMs, and iron materials.
(2) The copper winding is carefully chosen to achieve a similar stator copper weight across the three models. Additionally, the fill factor remains constant, and flat winding is used for all three.
(3) To compare the performances accurately, a 2D FEM analysis is conducted for all models. Considering different core saturations, the current angle at the maximum torque per ampere (MTPA) point is determined [23]. It is worth noting that models with hairpin windings require welding points, resulting in longer end-windings both axially and circumferentially. The phase resistance of each model is calculated using ANSYS RMxprt.

Table 1. Permanent magnet motor performance Requirements.

Item	Unit	Basic Model	Model 2	Model 3
Stator out dia.	mm		180	
Turns per slot	-		6	
Slot size (length/width)	mm		14.5/3.8	
Coil size (length/width)	mm		2.8/1.68	
Phase resistance at 20C	mΩ		19.45	
Rotor out dia.	mm		118.6	
Stack length	mm		150	
Air-gap thickness	mm		0.8	
PM size (length/width)	mm		16.2/5	
PM grade	-		G45UH	
Parallel branches	-		2	
Steel lamination	-		27PNX1300	
CFRP application	-	None	CFRP sleeve 0.5 mm	Molded CFRP

3. Open-Circuit Analysis of IPMSM

The phase-no-load back electromotive force (B-EMF) characteristics of the three models are shown in Figure 3a. These values were calculated using Equation (1).

$$e = \frac{K_e \omega_m N \Phi_p}{\pi a} \tag{1}$$

where K_e is the B-EMF constant, ω_m is the rotor angular velocity, N is the number of winding turns, Φ_P is the effective magnet flux passing through the coil, and a is the number of parallel circuits. Compared to the IPMSM basic model, model 2 with CFRP sleeve reduces the air-gap magnetic flux Φ_P due to the increase in effective air-gap thickness, but the leakage flux reduces more from the PM to the q-axis without the ribs and bridge structures. Therefore, the value of B-EMF increased. In addition, model 3 uses injection-molded CFRP materials, which reduce leakage flux while maintaining the same air-gap thickness as the basic model and model 2. This results in the highest B-EMF. To evaluate the sinusoidal quality of the no-load B-EMF, fast Fourier transform (FFT) analysis was used. As shown in Figure 3b, model 3 showed the largest fundamental component of the no-load B-EMF. In model 3, the dominant no-load B-EMF harmonics of the 11th order were high. The harmonic distortions of the B-EMF for the basic model and models 2–3 were 3.94%, 4.16%, and 12.52%, respectively. These values were calculated using the following equation:

$$THD = \frac{\sqrt{E_2^2 + E_3^2 + E_4^2 + \dots}}{E_1} \cdot 100\% \tag{2}$$

where E_1 is the fundamental component of the B-EMF, and E_2, E_3, and E_4 are the second, third, and fourth harmonics of the B-EMF, respectively. Figure 4 shows the comparison of the cogging torque among the three models. The cogging torque is the torque generated to minimize the reluctance between the rotor PM and the stator lamination. The value of the cogging torque is proportional to the amount of magnetic flux and inversely proportional to the air-gap thickness. The cogging torque can be calculated using the following equation:

$$T_{cogging} = -\frac{1}{2}\Phi_g^2 \frac{dR}{d\theta} \tag{3}$$

where Φ_g is the air-gap magnetic flux, and R is the reluctance. Based on the same principle, compared to the basic model, the absence of rib and bridge structures in model 2 leads to significant changes in reluctance, while the absence of a skew structure in model 3 further increases the cogging torque.

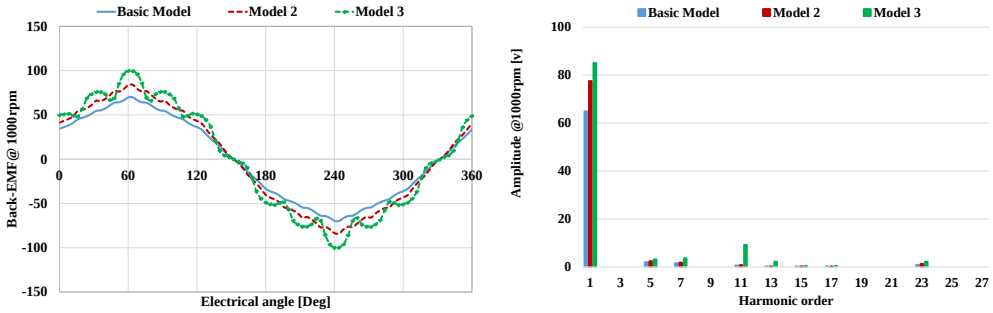

(**a**) (**b**)

Figure 3. (**a**) Line B-EMF of the three models. (**b**) FFT analysis of the three models.

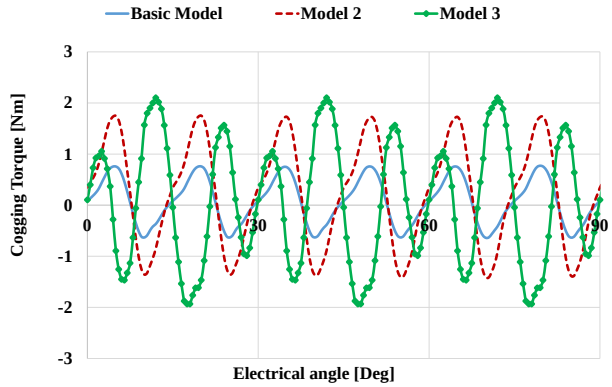

Figure 4. Cogging torque for the three models.

The proposed basic model exhibited the lowest peak-to-peak (pk2pk) cogging torque value, of 1.43 Nm, and the cogging torque was relatively small for model 2. The simulation results indicate the following trends. Compared to the base model, model 3, without a skew structure, will concentrate the magnetic flux in the air gap, resulting in an increase in cogging torque of 2.85 Nm. This is because the skew structure helps to reduce the magnetic field harmonics that cause cogging torque. The increase in cogging torque can cause vibration and noise, which can be a problem for some applications. Therefore, it is important to optimize the design of the motor to minimize the cogging torque.

4. Load-Operation Analysis of IPMSM

4.1. Comparison of Performance

The electromagnetic torque of the three models was evaluated using ideal sinusoidal current excitation. To compare the models' performances, we need to determine the current angle at the MTPA point, considering different core saturations. The MTPA point data at a base speed of 3000 r/min are listed in Table 2. Figure 5 illustrates the electromagnetic torque for the three models, while Figure 6 shows the load-operation magnetic-field distribution. It is important to note that not only is the rotor lamination significantly different, but the stator core saturation of the IPMSM also varies under load operation (as shown in Figure 6). Consequently, the MTPA point does not occur at the same angle for all the models. Additionally, the torque-ripple factor, defined as the ratio of the pk2pk torque to the average torque, was used to calculate the torque ripple. The expression for the torque-ripple factor is:

$$K_T = \frac{T_{\max} - T_{\min}}{T_{ATG}} \tag{4}$$

Table 2. 2D fem analysis results.

Item	Unit	Basic Model	Model 2	Model 3
Maximum speed	r/min		12,000	
Phase current (*Ia*)	A_{rms}		250	
	Open-Circuit Analysis @ 1000 r/min			
No-load B-EMF	V_{rms}	45.8	54.7	60.5
THD of-EMF	%	3.94	4.16	12.52
Cogging torque	Nm	1.43	3.16	4.28
	Load-Operation Analysis @3000 r/min			
Current angle (β)	deg	38	28	34
Torque	Nm	225.5	239.0	261.6
Torque ripple	%	6.9	9.8	28.3
Efficiency	%	93.4	93.8	94.2

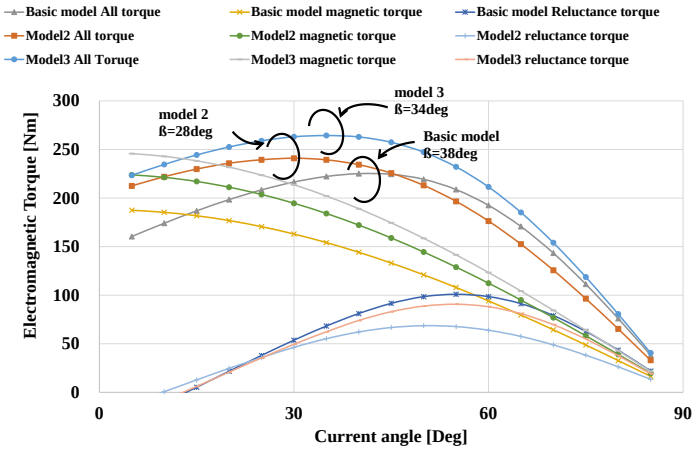

(**a**)

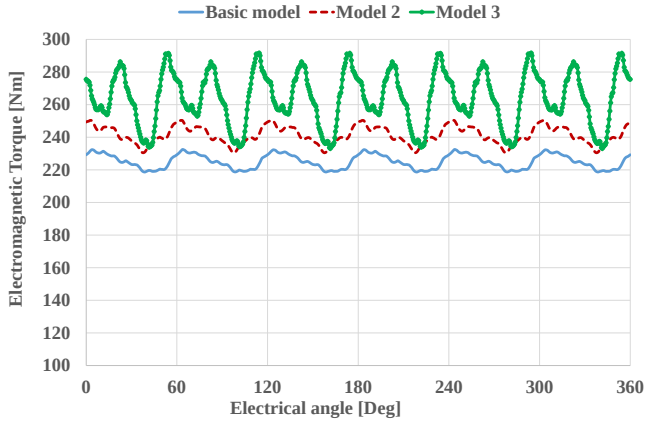

(**b**)

Figure 5. (**a**) FEM torque values at different current angles (phase current Ia: 250 Arms). (**b**) FEM torque waveform at rated operating point (current angle basic model, β: 38° model 2, β: 28° and model 3, β: 34°).

Because the air-gap fields contain harmonics from the rotor without ribs, the opening and shoes are derived from the high-magnetomotive-force-space harmonic content. Consequently, a large torque ripple is generated. These harmonics induce parasitic perturbations in the Maxwell stress, leading to a significant torque ripple in the CFRP-application model 2 and model 3 in comparison with basic model [24]. Despite this, both model 2 and model 3 exhibit higher maximum electromagnetic torque due to their increased air-gap magnetic density. The resulting tangential stress distribution on the rotor surface for the

field harmonics (denoted as "v") at a specific time instant around the air-gap periphery can be expressed as:

$$\sigma_\theta(\theta) = \frac{1}{\mu_0} \sum_{v=1}^{\infty} B_{\theta 0 v}(\theta) B_{rv}(\theta) \cos(\varphi_{dv}) \quad (5)$$

where $B_{\theta v}$ and B_{rv} are the harmonic field magnitudes and φ_{dv} is the angle between the two components.

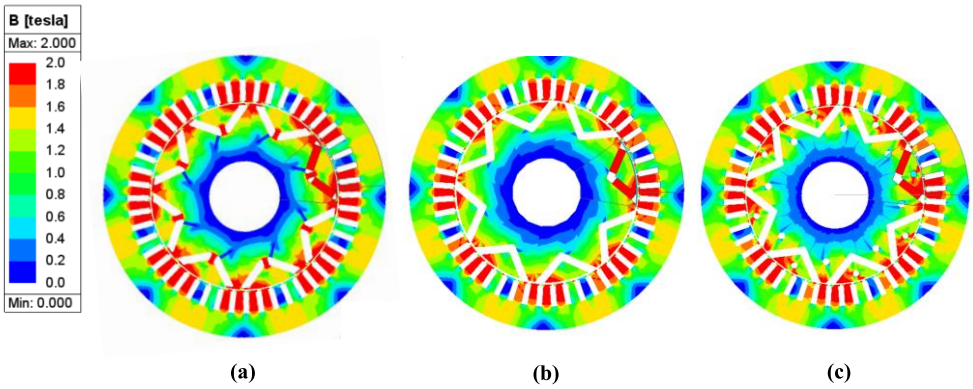

Figure 6. Cross-section and flux density distributions of three IPMSM models in MPTA conditions. (**a**) Basic model, load condition (Ia: 250 Arms, β: 38°). (**b**) Model 2, load condition (Ia: 250 Arms, β: 28°). (**c**) Model 3, load condition (Ia: 250 Arms, β: 34°).

Figure 7a compares the torque characteristics according to speed. The analysis shows that model 3 had the highest base torque (261.6 Nm) due to the absence of ribs and bridges on each pole. Compared to model 2, model 3 also had the highest torque density due to the elimination of the CFRP sleeve on the pole pieces. However, in the high-speed field weakening and the maximum torque per voltage (MTPV) control range, model 3 exhibited a rapid torque drop at high speeds (7000–12,000 r/min). This was attributed to a decrease in the actual magnetic leakage under the voltage limit. Figure 7b compares the efficiency characteristics according to speed. Due to the minimized flux leakage, model 3 exhibits the largest torque density and the highest efficiency in the MTPA range. However, a larger field-weakening current is required in the field-weakening and MTPV ranges, which reduces efficiency.

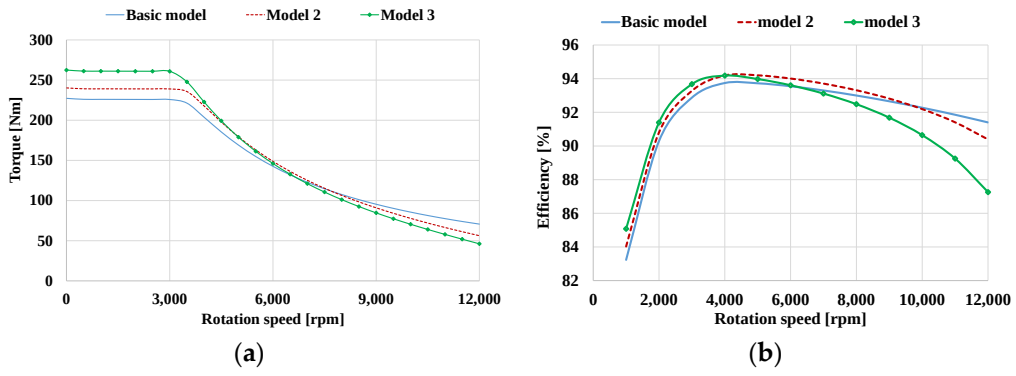

Figure 7. (**a**) Comparison of torques according to speed. (**b**) Comparison of efficiencies according to speed.

4.2. Comparison of Costs

The manufacturing cost is mostly influenced by the shape and volume of the PM. As discussed above, this study was designed to increase the manufacturing efficiency and torque density by using CFRP materials. To achieve an MTPA with higher electromagnetic torque, model 3 significantly increased its torque density and decreased its copper loss.

Compared to the basic model and model 2, model 3 increased the electromagnetic torque by 9.4% and 16.0%, respectively. This is equivalent to reducing the active parts' stack lengths by 24 mm and 14 mm for a model with a lamination length of 150 mm.

However, these performance improvements featured trade-offs. Model 3 required increased amounts of injection-molded CFRP materials and additional consumables for the injection process, which lead to potentially higher material costs. Specialized manufacturing techniques might also be needed for processing these materials. While the strength-to-weight ratio of CFRP makes its weight impact minimal, the overall cost increase might hinder its adoption in some applications. Therefore, a careful consideration of performance gains versus cost implications is crucial when selecting this design.

4.3. Comparison of the Efficiency Maps and WLTP Class 3 Driving Cycle

The motoring efficiency maps for the three models are shown in Figure 8. It should be noted that both model 2 and model 3 reduced the active part stack length to achieve the same maximum torque as the basic model, facilitating a direct comparison of their performances. The peak efficiency for model 1 is 96.8%, with a large 96% efficiency contour from 3000~6000 r/min; the high-efficiency region is well placed at low-to-medium torque levels and corresponds well to the typical drive cycle residency plot. Compared to model 1, model 3 exhibits a 0.5% decrease in maximum efficiency, reaching 96.3%. While its high-efficiency range also decreases, this aligns with the expected trade-off for reducing the active part length by 24 mm. Therefore, this reduction is considered acceptable. Notably, model 2's efficiency level falls between those of the basic model and model 3.

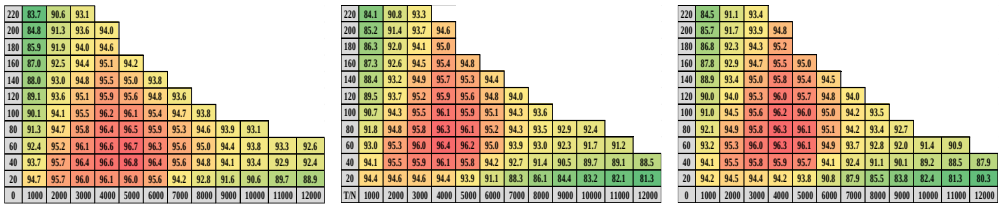

Figure 8. Efficiency map of three models. (**a**) Basic model, active part stack length 150 mm; (**b**) model 2, active part stack length 136 mm (9.4% reduction); (**c**) model 3, active part stack length 126 mm (16% reduction).

The three motors are compared in terms of energy consumption, with reference to the Worldwide Harmonized Light Vehicles Test Procedure (WLTP) class 3, which is a specific category within the global WLTP testing program designed for high-performance light-duty vehicles, particularly EVs with top speeds exceeding 130 km/h [25–27]. The motor speed, absolute load torque, and power over the WLTP are shown in Figure 9. The vehicle data are reported in the Appendix A. The EV propulsion motor specifications for temporary (peak) torque versus speed are shown in Figure 10a. From Figure 10a, it can be seen that all the operating points that can possibly occur for the WLTP class 3 driving cycle fall within the specified torque–speed envelopes of the motor. Therefore, provided that the continuous and temporary overload torque–speed curves are satisfied, the whole WLTP class 3 driving cycle operating points are achievable.

The results, in watts per hour, are shown in Figure 10b and refer to regenerative braking conditions. Only motor loss is considered here: The other loss components of the power train, which are those of the battery and the power converters, are outside of this comparison.

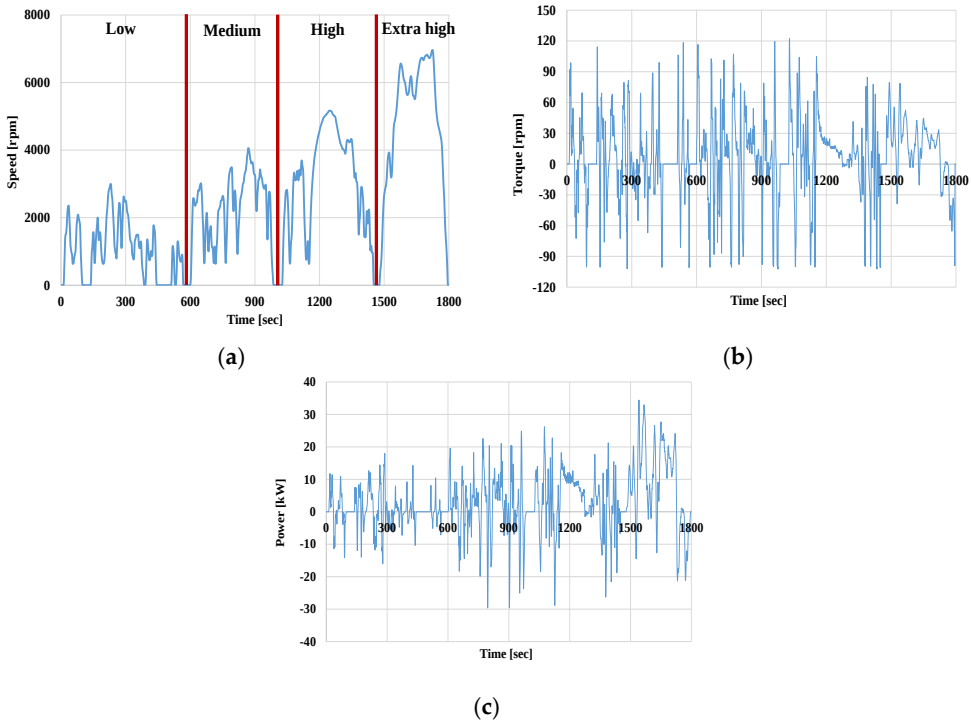

Figure 9. (**a**) Motor speed, (**b**) absolute load torque, and (**c**) power over the WLTP class 3 driving cycle.

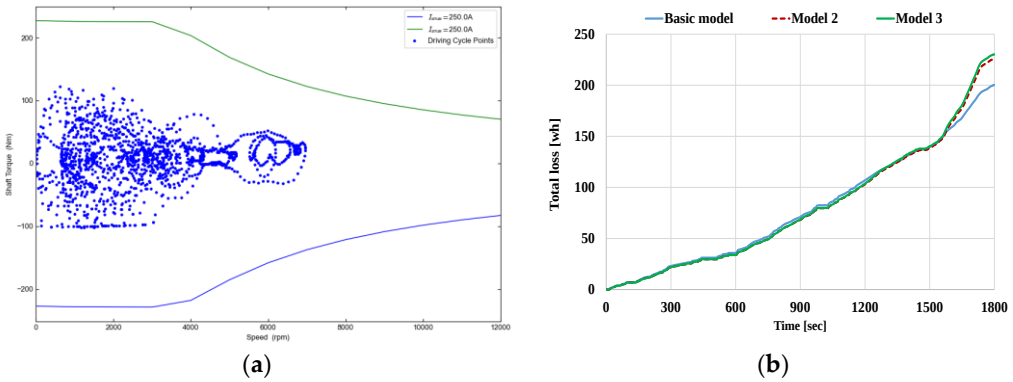

Figure 10. (**a**) EV-propulsion motor specification for peak torque versus speed characteristics (basic model); (**b**) energy loss over the WLTP class 3 for the three models, basic model (stack length 150 mm), model 2 (stack length 136 mm), and model 3 (stack length 126 mm).

The three models exhibit similar performance levels during the initial cycle segment, representing urban driving conditions (low and medium WLTP ranges). Interestingly, despite having significantly shorter stack lengths, the modified models 2 and 3 achieve greater torque density thanks to the reduced magnetic flux leakage. This translates to lower copper losses compared to the base model in this urban driving condition. However, during simulated suburban and high-speed driving (from 1300 s onwards), the performance of the modified models 2 and 3 suffers. As previously mentioned, these models have greater linkage flux, requiring a larger field-weakening current to maintain high speeds. Consequently, their energy consumption rapidly increases within the high and extra-high WLTP ranges. The energy loss in each range is confirmed in Table 3.

Table 3. Energy loss over the wltp class 3 for the three models.

Item	Unit	Basic Model	Model 2	Model 3
WLTP low-range loss	Wh	36.2	34.2	34.2
WLTP medium-range loss		39.4	39	39.3
WLTP high-range loss		61.4	63.3	64.5
WLTP extra-high-range loss		63.2	89.4	92.2

5. Stress Analysis of IPMSM

Finally, in order to verify the correctness of the analytical method, the strength of the three models' rotor is analyzed and verified by FEM. The safety factor can be calculated as

$$k_{safe} = \frac{\sigma_{Yield}}{\sigma_E} \tag{6}$$

$$\sigma_E = \frac{\sqrt{(\sigma_x - \sigma_y)^2 + (\sigma_y - \sigma_z)^2 + (\sigma_z - \sigma_x)^2 + 6(\sigma_{xy}^2 + \sigma_{yz}^2 + \sigma_{zx}^2)}}{\sqrt{2}} \tag{7}$$

where σ_{Yield} is the yield strength, σ_{E} is the equivalent stress, and σ_{x}, σ_{y}, σ_{z}, σ_{xy}, σ_{yz}, and σ_{zx} are the direct stress components. Equivalent stress is used in design work because it allows any arbitrary three-dimensional stress state to be represented as a single positive stress value. Equivalent stress is part of the maximum equivalent stress failure theory used to predict yielding in ductile materials. Figure 11 shows the stress analysis results of the three models.

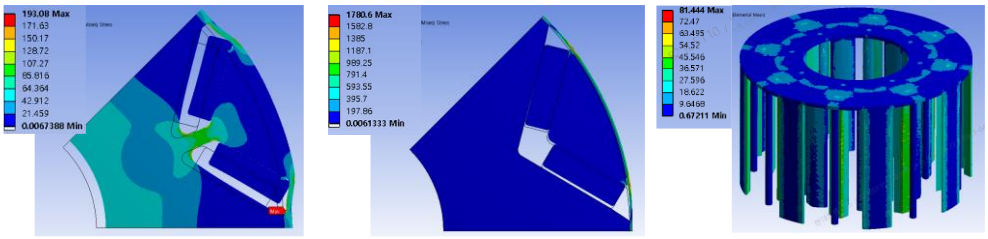

(**a**) (**b**) (**c**)

Figure 11. Stress analysis of a candidate design model at 12,000 r/min. (**a**) Basic model. (**b**) model 2. (**c**) model 3.

As the yield strength of the electric steel and CFRP materials used in this study is shown in Table 4, the safety factor can also be confirmed from Table 4. The results show that while the safety factors of the basic model (2.8) and model 2 (2.0) are within an acceptable range, model 3's factor (6.0) exceeds the target. To optimize the design and potentially reduce material costs, future studies could explore lowering the injection-molded CFRP materials' contents while maintaining structural integrity. Additionally, the thermal properties of CFRP injection-molded composite materials need to be considered. The thermal performance of the CFRP composite material is shown in Table 5. Since composite materials are not good conductors of heat, they are not conducive to the heat dissipation of PMs. Under high-speed conditions, it is necessary to analyze the temperature of the motor's PMs separately. Furthermore, permanent magnets can withstand significant compressive stress, but they cannot withstand large tensile stress. To ensure that the permanent magnets do not become loose under high-speed rotor-rotation conditions, the CFRP-injection-molded composite materials' injection speed needs to be considered to avoid cracks and pores during stamping, which would reduce the strength. The thermal properties of composite materials are significantly higher than the operating temperatures of PMs, so there is no need to worry about thermal deformation.

Table 4. Physical properties and 2d stress analysis results.

Item	Unit	Electrical Steel (27PNX1300)	CFRP Sleeve (T300)	CFRP Injection (PPA-CF40)
Density	g/cm^3	7.65	1.76	1.33
Elastic modulus	GPa	178	230	34.5
Tensile strength	MPa	547	3530	490
Stress analysis at 20,000 r/min		Basic model	Model 2	Model 3
Stress (Von-Mises)	MPa max	193.1	1780.6	81.4
Safety factor	-	2.8	2.0	6.0

Table 5. Thermal properties of PPA-CF40.

Item	Unit	Value
Heat deflection Temp.	°C	287
Melting Temp.	°C	300
Thermal conductivity	W/(mk)	0.45

6. Conclusions

This paper proposes and studies a drive motor that incorporates injection-molded carbon fiber and conducts a comprehensive comparison with a carbon-fiber wound motor and a basic model motor. Our findings demonstrate a significant improvement in torque density for the injection-molded carbon fiber motor. Notably, removing the rotor ribs and bridges effectively reduces the leakage flux bypassing the air gap, as evidenced by a higher no-load back electromotive force. This translates to superior performance across the motor's MTPA range and at low speeds with high torque. However, these changes also introduce some drawbacks. For instance, increased torque ripples and greater copper losses at high speeds lead to reduced efficiency. Addressing these limitations presents promising avenues for future research, such as:

1. Designing stators with complementary inclined grooves.
2. Developing models for fabricating inclined grooves, considering factors like injection-molding strength, air bubbles, and non-connection during the process.

Despite the increased torque density achieved by the injection-molded carbon-fiber motor compared to the basic model, the motor necessitates additional CFRP material and injection-molding consumables, potentially translating to higher costs. Future studies should delve deeper into the trade-offs between manufacturing complexity and affordability.

Author Contributions: Conceptualization, H.C.L.; Methodology, J.S.P.; Writing—original draft, H.C.L.; Writing—review & editing, H.C.L.; Project administration, I.H.A. All authors have read and agreed to the published version of the manuscript.

Funding: This research was funded by the Technology Innovation Program (20015779, Development of multi-drive motor AWD system technology based on multi-safety design) supported by the Ministry of Trade, Industry & Energy (MOTIE, Republic of Korea).

Data Availability Statement: The original contributions presented in the study are included in the article, further inquiries can be directed to the corresponding author.

Conflicts of Interest: Huai Cong Liu, Jang Soo Park, and Il Hwan An are employees of Hyundai-transys. The paper reflects the views of the scientists, and not the company.

Appendix A

The vehicle data used for evaluating the WLTP class 3 in Section 2 are reported in Table A1.

Table A1. Vehicle specification.

Item	Unit	Value
Vehicle mass	kg	1360
Rolling resistance coefficient	-	0.0054
Frontal area	mm^2	1.746
Drag coefficient	-	0.26
Gear ratio	-	6
Wheel radius	m	0.3
Transmission efficiency	-	0.97
Max. vehicle speed	km/h	180

References

1. Kim, K.-O.; Jung, Y.-H.; Park, J.-C.; Lim, M.-S. Comparative Study of Mechanical and Electrical Characteristics of High-Strength and Conventional Electrical Steel for EV Traction High-Speed Multilayer IPMSM Using Rare-Earth Free PM. *IEEE Trans. Magn.* **2023**, *59*, 8102205. [CrossRef]
2. Gerada, D.; Mebarki, A.; Brown, N.; Gerada, C.; Cavagnino, A.; Boglietti, A. High-speed electrical machines: Technologies, trends, and developments. *IEEE Trans. Ind. Electron.* **2014**, *61*, 2946–2959. [CrossRef]
3. Lee, S.-H.; Song, S.-W.; Kim, D.-H.; Min, J.-Y.; Kim, W.-H. Performance comparison analysis and process suggestion through slot less SPMSM during high-speed operation. *AIP Adv.* **2023**, *13*, 025039. [CrossRef]
4. Wang, L.; Du, G.; Tong, J.; Huang, N.; Hu, C.; Xu, W. Comparation of Different Rotor Sleeves of Highspeed Permanent Magnet Synchronous Motors Based on Multi-physics. In Proceedings of the 2021 IEEE 4th Student Conference on Electric Machines and Systems (SCEMS), Huzhou, China, 1–3 December 2021; pp. 1–5.
5. Ciampolini; Fazzini; Berzi; Ferrara; Pugi, L. Simplified Approach for Developing Efficiency Maps of High-Speed PMSM Machines for Use in EAT Systems Starting from Single-Point Data. In Proceedings of the 2020 IEEE International Conference on Environment and Electrical Engineering and 2020 IEEE Industrial and Commercial Power Systems Europe, EEEIC, Madrid, Spain, 9–12 June 2020; pp. 1–6.
6. Zhang, J.; Chen, W.; Huang, X.; Fang, Y.; Zhang, J.; Ma, J.; Cao, W. Evaluation of applying retaining shield rotor for high-speed interior permanent magnet machines. *IEEE Trans. Magn.* **2015**, *51*, 8100404.
7. Du, G.-H.; Li, N.-M.; Zhou, Q.-X.; Gao, W.-T.; Wang, L.; Pu, T. Multi-Physics Comparison of Surface-Mounted and Interior Permanent Magnet Synchronous Motor for High-Speed Applications. *Machines* **2022**, *10*, 700. [CrossRef]
8. Li, Y.; Wang, Y.-W.; Zhang, Z.-R.; Li, J.-C. Investigation and Development of the Brushless and Magnet less Wound Field Synchronous Motor Drive System for Electric Vehicle Application. *World Electr. Veh. J.* **2023**, *14*, 81. [CrossRef]
9. Aiso, K.; Akatsu, K. Performance Comparison of High-Speed Motors for Electric Vehicle. *World Electr. Veh. J.* **2022**, *13*, 57. [CrossRef]
10. Yang, Z.; Shang, F.; Brown, I.P.; Krishnamurthy, M. Comparative Study of Interior Permanent Magnet, Induction, and Switched Reluctance Motor Drives for EV and HEV Applications. *IEEE Trans. Transp. Electrif.* **2015**, *1*, 245–254. [CrossRef]
11. Ahn, J.-H.; Han, C.; Kim, C.-W.; Choi, J.-Y. Rotor Design of High-Speed Permanent Magnet Synchronous Motors Considering Rotor Magnet and Sleeve Materials. *IEEE Trans. Appl. Supercond.* **2018**, *28*, 5201504. [CrossRef]
12. Shen, J.-X.; Hao, H.; Jin, M.-J.; Yuan, C. Reduction of Rotor Eddy Current Loss in High Speed PM Brushless Machines by Grooving Retaining Sleeve. *IEEE Trans. Magn.* **2013**, *49*, 3973–3976. [CrossRef]
13. Zhang, F.; Du, G.; Wang, T.; Liu, G.; Cao, W. Rotor retaining sleeve design for a 1.12-MW high-speed PM machine. *IEEE Trans. Ind. Appl.* **2015**, *51*, 3675–3685. [CrossRef]
14. Zhou, F.Z.; Shen, J.X.; Fei, W.; Lin, R. Study of retaining sleeve and conductive shield and their influence on rotor loss in high-speed PM BLDC machines. *IEEE Trans. Magn.* **2006**, *42*, 3398–3400. [CrossRef]
15. Han, T.; Wang, Y.; Shen, J.-X. Analysis and Experiment Method of Influence of Retaining Sleeve Structures and Materials on Rotor Eddy Current Loss in High-Speed PM Motors. *IEEE Trans. Ind. Appl.* **2020**, *56*, 4889–4895. [CrossRef]
16. Olsen, L.E.; Nelson, D.; Laskaris, K.; GE, H.; Filip, E.; Vega, C.; Pellerey, P.; Papanikolaou, V. Permanent Magnet Motor with Wrapping. U.S. Patent Publication No. WO2021225902A1, 11 November 2021.
17. KevinGrace; Galioto, S.; Bodla, K.; El-Refaie, A. Design and Testing of a Carbon Fiber Wrapped Synchronous Reluctance Traction Motor. *IEEE Trans. Ind. Appl.* **2018**, *54*, 4207–4217. [CrossRef]
18. Zhang, F.; Du, G.; Wang, T.; Wang, F.; Cao, W.; Kirtley, J.L. Electromagnetic design and loss calculations of a 1.12-MW high-speed permanent-magnet machine for compressor applications. *IEEE Trans. Energy Convers.* **2016**, *31*, 132–140. [CrossRef]
19. Kawabe, K.; Sasayama, H.; Tomoda, S. New Carbon Fiber Tow-Spread Technology and Applications to Advanced Composite Materials. *Sampe J.* **2009**, *45*, 6–17.
20. Katagiri, K.; Sasaki, K.; Honda, S.; Nakashima, H.; Yamaguchi, S.; Ozaki, T.; Sonomura, H.; Kakitsuji, A. CFRP manufacturing method using electrodeposition resin molding for curvilinear fiber arrangements. *Compos. Part A Appl. Sci. Manuf.* **2017**, *102*, 108–116. [CrossRef]

21. Mitsubishi Chemical Corporation Document. Available online: https://www.m-chemical.co.jp/carbon-fiber/en/about/molding/ (accessed on 19 February 2024).
22. Hwang, M.-H.; Han, J.-H.; Kim, D.-H.; Cha, H.-R. Design and Analysis of Rotor Shapes for IPM Motors in EV Power Traction Platforms. *Energies* **2018**, *11*, 2601. [CrossRef]
23. Liu, H.C.; Joo, K.J.; Oh, Y.J.; Lee, H.J.; Seol, H.S.; Jin, C.S.; Kim, W.H.; Lee, J. Optimal Design of an Ultra-Premium-Efficiency PMA-Synchronous Reluctance Motor with the Winding Method and Stator Parameters to Reduce Flux Leakage and Minimize Torque Pulsations. *IEEE Trans. Magn.* **2018**, *54*, 8207505. [CrossRef]
24. Liu, H.-C.; Lee, H.-J.; Seol, H.-S.; Cho, S.-Y.; Lee, J.; Oh, Y.-J. Optimal Slot Design of IPMSM in Railway with Independently Rotating Wheelsets. *IEEE Trans. Magn.* **2019**, *55*, 8200404. [CrossRef]
25. Hwang, S.-W.; Ryu, J.-Y.; Chin, J.-W.; Park, S.-H.; Kim, D.-K.; Lim, M.-S. Coupled Electromagnetic-Thermal Analysis for Predicting Traction Motor Characteristics according to Electric Vehicle Driving Cycle. *IEEE Trans. Veh. Technol.* **2021**, *70*, 4262–4272. [CrossRef]
26. Mahmouditabar, F.; Baker, N.J. Design Optimization of Induction Motors with Different Stator Slot Rotor Bar Combinations Considering Drive Cycle. *Energies* **2024**, *17*, 154. [CrossRef]
27. Muazzam, H.; Ishak, M.K.; Hanif, A.; Bhatti, A.I. Compensating Thermal Derated Torque of IPMSM Centric Electric Vehicles. *IEEE Access* **2022**, *10*, 22468–22480. [CrossRef]